

This is an Open Access document downloaded from ORCA, Cardiff University's institutional repository:<https://orca.cardiff.ac.uk/id/eprint/138744/>

This is the author's version of a work that was submitted to / accepted for publication.

Citation for final published version:

Ai, Congfang, Ma, Yuxiang, Yuan, Changfu, Xie, Zihua and Dong, Guohai 2021. A three-dimensional non-hydrostatic model for tsunami waves generated by submarine landslides. *Applied Mathematical Modelling* 96 , pp. 1-19. 10.1016/j.apm.2021.02.014

Publishers page: <http://dx.doi.org/10.1016/j.apm.2021.02.014>

Please note:

Changes made as a result of publishing processes such as copy-editing, formatting and page numbers may not be reflected in this version. For the definitive version of this publication, please refer to the published source. You are advised to consult the publisher's version if you wish to cite this paper.

This version is being made available in accordance with publisher policies. See <http://orca.cf.ac.uk/policies.html> for usage policies. Copyright and moral rights for publications made available in ORCA are retained by the copyright holders.



A three-dimensional non-hydrostatic model for tsunami waves generated by submarine landslides

Congfang Ai^a, Yuxiang Ma^{a,*}, Changfu Yuan^a, Zhihua Xie^b, Guohai Dong^a

^a*State Key Laboratory of Coastal and Offshore Engineering, Dalian University of Technology, Dalian 116024, China*

^b*Hydro-environmental Research Centre, School of Engineering, Cardiff University, Cardiff CF10 3AT, United Kingdom*

Abstract: A three-dimensional (3D) non-hydrostatic model for simulating nonlinear and dispersive waves is extended to compute submarine-landslide-generated waves. The model uses a projection method to solve the 3D Navier-Stokes equations on a 3D grid system built from a two-dimensional (2D) horizontal mesh by adding several horizontal layers in the vertical direction. The free surface is efficiently captured by the so-called free surface equation. The bottom movement is incorporated in the model by specifying the kinematic boundary condition at the impermeable bottom. The extension does not alter the property of the discretized Poisson equation for non-hydrostatic pressure correction terms. Thus, it can be also solved efficiently by the preconditioned conjugate gradient method. A wide range of tests including 2D and 3D landslide waves are simulated. Comparisons between numerical results and experimental data and/or other model results are presented. It is found that a good agreement has been obtained for a range of landslide waves using a very small number of horizontal layers (e.g. three or five layers) and the proposed model can be considered as an attractive alternative to simulating submarine-landslide-generated waves.

Keywords: Three-dimensional; Non-hydrostatic; Submarine landslide; Tsunami waves; Navier-Stokes equations

1. Introduction

It is well-known that submarine landslide is one of the mechanisms contributing to

the formation of tsunami waves, whether in coastal areas or in closed water basins such as bays and lakes. They usually have destructive effects on human communities and vital infrastructures and have been studied by a large number of physical experiments. Many early numerical models for tsunami waves are developed based on shallow water theory [1]. However, with the availability of fast computers, many efforts have been sought to obtain nonlinear and dispersive numerical models, because nonlinearity and dispersion play very important roles in the generation and propagation of tsunami waves [1-3].

The existing numerical models for predicting landslide-generated dispersive waves can be mainly classified into three groups: Boussinesq-type models [2,4,5], potential flow models [6–9], and models based on the Navier-Stokes equations (NSE) [10–16]. Boussinesq-type models are depth-integrated and thus can be solved efficiently across a large spatial domain. Nevertheless, the feature of high-order, mixed derivative terms in these models complicates the discretized methods, particularly in complex spatial domains. Potential flow models are derived from the incompressible NSE, but they have limited application due to the assumption of perfect fluid and irrotational motion. Although numerical results based on the Boussinesq-type models and the potential flow models have been shown to give generally good predictions for a range of tsunami waves generated by landslides, models based on NSE are the most advanced numerical models and have the potential for accurately simulating tsunami waves by incorporating complicated turbulence models. However, large computational expense is the key problem to be solved for NSE-based models.

At present, most NSE-based numerical models for landslide tsunami waves employ the volume of fluid (VOF) method [10,12–14] or smoothed particle hydrodynamics (SPH) method [11,15,16] to capture the free surface. These models are capable of predicting overturning free surface flows, but their further applications are limited by the high computational expense. As for free surface flows in which the free surface elevation can be defined as a single-valued function of horizontal positions, the so-called free surface equation can be used to calculate the moving

surface, which is used in non-hydrostatic models. Thus with relatively small computational expense, these models are capable of accurately predicting a wide variety of wave motions.

Non-hydrostatic models for water wave dynamics have been used [17–24] for nearly 20 years. These models can be applied to simulate various problems involving dispersive waves or non-hydrostatic effects. The tsunami wave generated by submarine landslides is one of these problems. In this paper, we will extend our non-hydrostatic model [18] to simulate submarine-landslide-generated waves and validate the developed model for a wide range of test cases. The previous non-hydrostatic model [18] employs a novel grid arrangement, which renders the Poisson equation efficiently solvable. Moreover, the model is capable of accurately resolving nearshore wave breaking and run-up [17] and even the focusing of wave groups [19]. The extension of the previous model [18] is carried out by incorporating the bottom movement to predict the moving landslide. The discretized Poisson equation for the developed model is still symmetric and can be solved efficiently by the preconditioned conjugate gradient method. To the best of our knowledge, several attempts have been made to apply non-hydrostatic models for simulating tsunami waves generated by landslides. One application was initiated by [22], who presented a shock-capturing non-hydrostatic model for the simulation of dispersive waves and validated it by only one case of landslide-generated tsunami. Ruffini et al. [25] investigated the effect of the water body geometry on landslide-tsunami propagation in the far field by using SWASH [24]. Hill et al. [26] predicted the Storegga Slide tsunami by using a non-hydrostatic developed model on a highly flexible finite-element/control-volume modelling framework. Pan et al. [27] presented two finite element non-hydrostatic models to simulate an example of 3D landslide-generated tsunami. In addition, there are also several non-hydrostatic models aimed at the prediction of tsunami waves generated by deformable [28, 29] or granular landslides [30, 31]. Grilli et al. [32] presented numerical simulations of the tsunami from the December 22, 2018 lateral collapse of Anak Krakatau volcano in the Sunda Straits, Indonesia with NHWAVE [22, 28, 30]. The main advantage of the

present non-hydrostatic model is that it can be solved efficiently because of the symmetric property of the Poisson equation.

The remainder of this paper is organized as follows. Section 2 presents the governing equations. The numerical algorithm used to solve the non-hydrostatic model is described in Section 3. Numerical validations and conclusions are provided in Section 4 and 5, respectively.

2. Governing equations

The 3D incompressible NSE are derived from the conservation of mass and momentum and can be expressed in the following form:

$$\frac{\partial u}{\partial x} + \frac{\partial v}{\partial y} + \frac{\partial w}{\partial z} = 0 \quad (1)$$

$$\frac{\partial u}{\partial t} + \frac{\partial u^2}{\partial x} + \frac{\partial uv}{\partial y} + \frac{\partial uw}{\partial z} + g \frac{\partial \eta}{\partial x} + \frac{\partial q}{\partial x} = \nu_t \left(\frac{\partial^2 u}{\partial x^2} + \frac{\partial^2 u}{\partial y^2} + \frac{\partial^2 u}{\partial z^2} \right) \quad (2)$$

$$\frac{\partial v}{\partial t} + \frac{\partial uv}{\partial x} + \frac{\partial v^2}{\partial y} + \frac{\partial vw}{\partial z} + g \frac{\partial \eta}{\partial y} + \frac{\partial q}{\partial y} = \nu_t \left(\frac{\partial^2 v}{\partial x^2} + \frac{\partial^2 v}{\partial y^2} + \frac{\partial^2 v}{\partial z^2} \right) \quad (3)$$

$$\frac{\partial w}{\partial t} + \frac{\partial uw}{\partial x} + \frac{\partial vw}{\partial y} + \frac{\partial w^2}{\partial z} + \frac{\partial q}{\partial z} = \nu_t \left(\frac{\partial^2 w}{\partial x^2} + \frac{\partial^2 w}{\partial y^2} + \frac{\partial^2 w}{\partial z^2} \right) \quad (4)$$

where t is the time; u , v and w are the velocity components in the horizontal x , y , and vertical z directions, respectively; $p = g(\eta - z) + q$ is the normalized pressure divided by a constant reference density and splitted into hydrostatic and non-hydrostatic ones; η is the free surface elevation; q is the non-hydrostatic pressure component; g is the gravitational acceleration; and ν_t is the eddy viscosity.

To predict submarine-landslide-generated waves, a moving bottom boundary is considered in the model and the vertical velocity component at the impermeable bottom $z = -h(x, y, t)$ is specified by the following kinematic bottom boundary condition:

$$w|_{z=-h} = -\frac{\partial h}{\partial t} - u\frac{\partial h}{\partial x} - v\frac{\partial h}{\partial y} \quad (5)$$

At the moving free surface $z = \eta(x, y, t)$, the kinematic boundary condition is expressed as:

$$w|_{z=\eta} = -\frac{\partial \eta}{\partial t} + u\frac{\partial \eta}{\partial x} + v\frac{\partial \eta}{\partial y} \quad (6)$$

Integrating the continuity equation (1) over the water column and applying the kinematic boundary conditions (5) and (6), the following so-called free-surface equation is obtained:

$$\frac{\partial(\eta + h)}{\partial t} + \frac{\partial}{\partial x} \int_{-h}^{\eta} u dz + \frac{\partial}{\partial y} \int_{-h}^{\eta} v dz = 0 \quad (7)$$

Notably, $-h(x, y, t)$ is a function of time and is determined by the pre-defined landslide motion.

The eddy viscosity ν_t is determined by the following Smagorinsky model [33]:

$$\nu_t = \nu + (C_s \Delta)^2 (2S_{ij}S_{ij})^{1/2}, \quad \Delta = (\Delta x \Delta y \Delta z)^{1/3} \quad (8)$$

where ν is the molecular viscosity; $C_s = 0.2$ is used in this study; Δx , Δy and Δz are grid sizes in the x , y and z directions, respectively; S_{ij} is the rate of strain. Notably, the Smagorinsky model is just used for numerical stability in this study.

3. Numerical algorithms

Following Ai et al. [18], a projection method is firstly used to solve Eqs. (1)-(4) in this model. This step can be divided into two stages. The first stage is performed by solving Eqs. (2)-(4) to get the intermediate velocities $u^{n+1/2}$, $v^{n+1/2}$ and $w^{n+1/2}$. In this stage, all the terms containing the non-hydrostatic pressure are discretized explicitly by means of finite difference and finite volume methods.

In the second stage, the discretized Poisson equation for non-hydrostatic pressure

correction terms is derived and solved. It is worth mentioning that the incorporation of the moving bottom boundary Eq. (5) in the model does not alter the property of the discretized Poisson equation. It is also symmetric and is solved efficiently by the preconditioned conjugate gradient method. Once the non-hydrostatic pressure correction term Δq is obtained, the new velocities u^{n+1} , v^{n+1} and w^{n+1} are computed by correcting the intermediate values after including Δq .

In the following step, the time derivative term of bottom topography $\frac{\partial h}{\partial t}$ is calculated according to the motion of the landslide. Then, based on the new velocity field, the vertical velocity component at the impermeable bottom $w^{n+1}|_{z=-h}$ and the new water surface elevation η^{n+1} are updated by applying finite volume discretizations to solve Eqs. (5) and (7), respectively. For more details about the numerical discretization, the reader is referred to Ai et al. [18].

In addition, it should be mentioned that the 3D grid system used in this model is built from a 2D horizontal structured mesh by just adding several vertical layers. A schematic diagram about the vertical grid system is illustrated in Fig. 1. In the vertical direction, to better fit the moving free surface and the complex bathymetry, a boundary-fitted coordinate system is employed. Therefore, the interface between two layers is defined as follows:

$$z_{k+1/2}(x, y, t) = z_{k-1/2}(x, y, t) + [\eta(x, y, t) + h(x, y, t)] / N_z, \quad k = 0, \dots, N_z \quad (9)$$

where k is the layer index; N_z is the number of vertical layers; $z_{1/2} = -h(x, y, t)$ and $z_{N_z+1/2} = \eta(x, y, t)$.

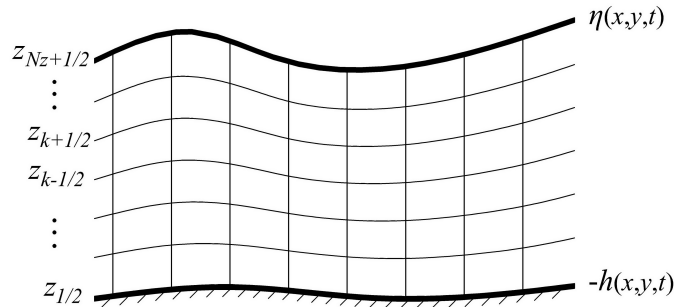


Fig. 1. The vertical boundary-fitted coordinate system

4. Model validation

To demonstrate the capability of the present non-hydrostatic model for accurately predicting tsunami events, five test cases are presented. The first four tests are essentially 2D vertical problems, which involve different bottom motions, while the final test presents tsunami waves generated by a 3D landslide and has been used as a typical 3D benchmark test. In all the simulations, the turbulent kinematic viscosity ν is calculated by Eq. (8), which can be easily implemented in this model, as presented by Ai and Jin [34]. It should be mentioned that the performance of the present model in resolving linear dispersion relations is presented by Ai et al. [18]. The present model with two horizontal layers can accurately predict linear dispersive waves up to $Kh_0 \leq 7$, where K is the wave number and h_0 is the still water depth.

4.1 Tsunami waves generated by impulsive bottom movements

Tsunami waves generated by impulsive bottom movements in a constant water depth were first studied numerically and experimentally by Hammack [35]. More recently, these experiments have been used for testing Boussinesq-type numerical models [2,5]. Hammack [35] considered two situations of bottom movement, namely, the impulsive upward motion and the impulsive downward motion (hereafter called the upward case and the downward case, respectively). The time-variable bottom topography is described as follows:

$$h(x, t) = h_0 - \zeta_0(1 - e^{-\alpha t})H(b^2 - x^2) \quad (10)$$

where $h_0 = 1.0$ m is the undisturbed water level; H is the Heaviside step function; $b = 12.2$ m is the step length measured from the upward boundary wall ($x = 0$); and $\alpha = 1.11/t_c$. For upward bottom movement, ζ_0 and t_c were set to 0.1 m and $0.148b/\sqrt{gh_0}$, respectively, while for the other case, they were taken as -0.1 m and $0.093b/\sqrt{gh_0}$, respectively.

In the two computations, the grid size used in the horizontal domain is $\Delta x = 0.25$

m, which is similar to that used in the Boussinesq-type model [5]. As a result, the length of the step length is discretized into approximately 50 cells. The time step is set to 0.05 s and only three layers are taken in the vertical direction. Figs. 2 and 3 compare the time histories of the computed free-surface elevations with the experimental data by Hammack [35] for the upward case and the downward case, respectively. Numerical results obtained by the high-order Boussinesq-type model [5] are also plotted for comparison. It can be found from Figs. 2 and 3 that the present model results are almost identical to those obtained by the Boussinesq-type model, although viscous energy dissipation is included by incorporating the Smagorinsky turbulence model in the study. Near the generation field of waves (Fig. 2a and b and Fig. 3a and b), the present model results are in good agreement with the experimental data, nevertheless very noticeable discrepancy between them can be found in the far-field waves (Fig. 2c and d and Fig. 3c and d). Due to the good agreement between the present viscous model and the Boussinesq-type model [5], it can be inferred in this study that the viscous terms play negligible role and the reason for the discrepancy between the present model results and the experimental data might be due to the friction losses caused by the boundary walls which were not considered in this study.

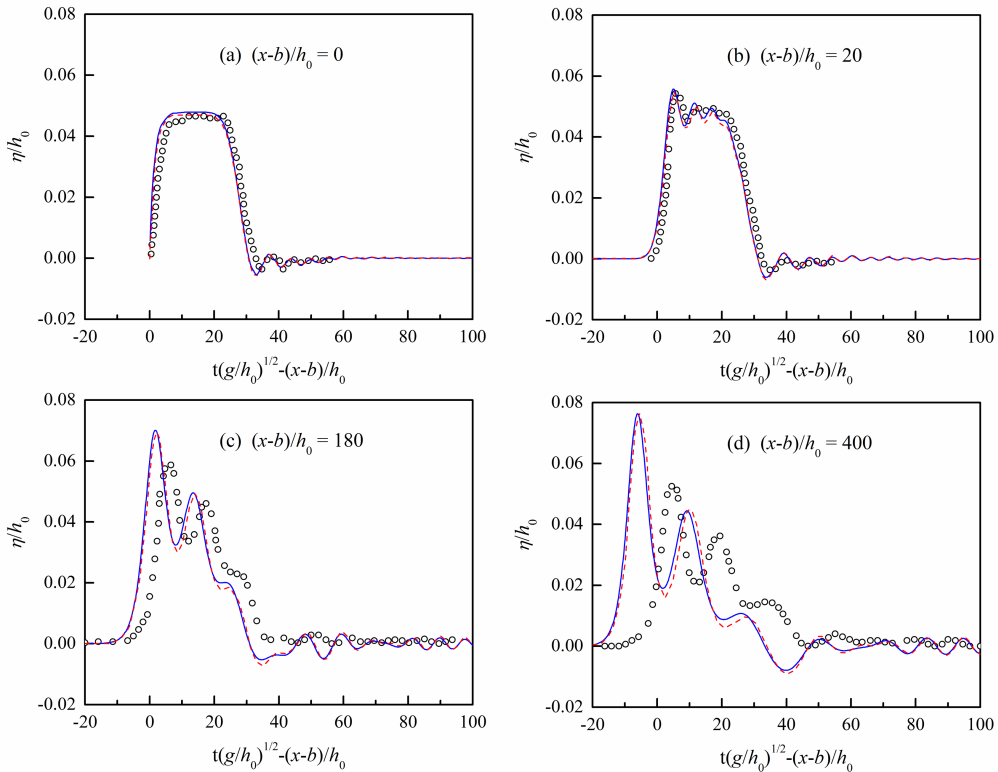


Fig. 2. Comparisons of time histories of the free-surface elevation at different locations between experimental data (open circles), the present model results (solid lines) and the numerical results obtained by the high-order Boussinesq-type model [5] (dashed lines) for the upward case.

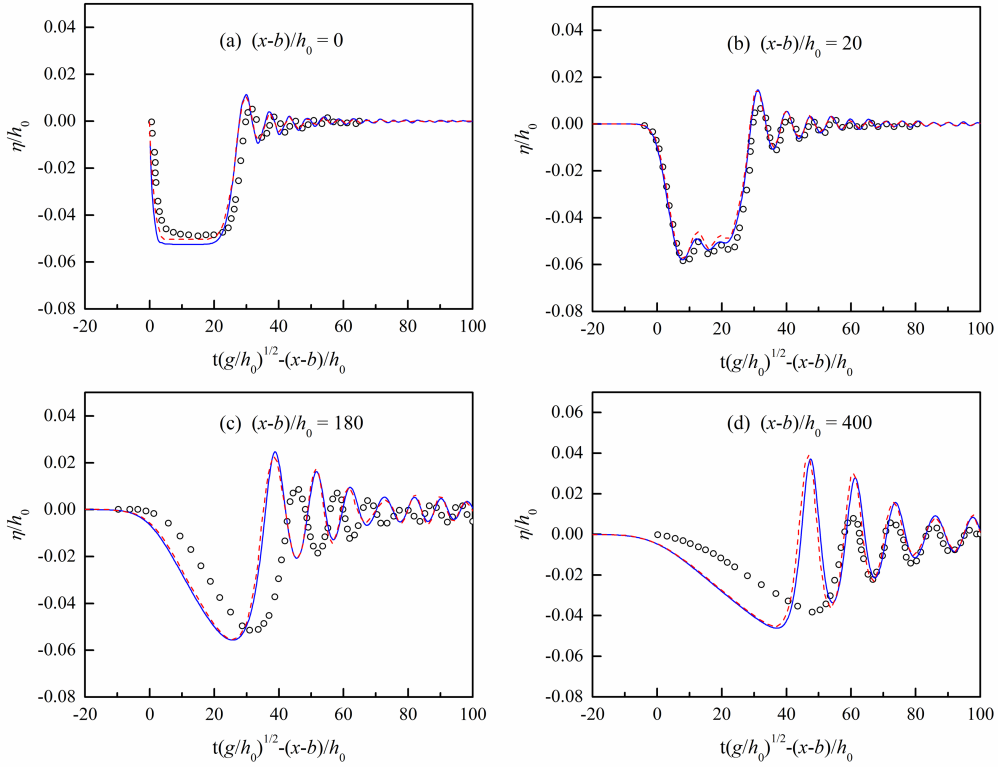


Fig. 3. Comparisons of time histories of the free-surface elevation at different locations between experimental data (open circles), the present model results (solid lines) and the numerical results obtained by the high-order Boussinesq-type model [5] (dashed lines) for the downward case.

4.2 Numerical tsunami wave of Lynett and Liu's [2]

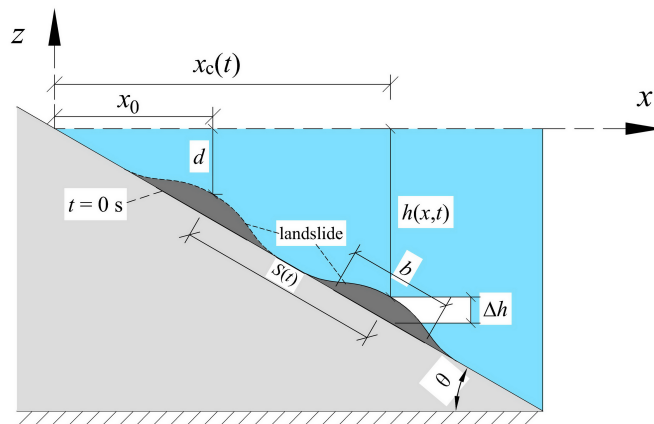


Fig. 4. Schematic diagram for the numerical set-up of Lynett and Liu [2].

Lynett and Liu [2] conducted a numerical simulation of a submarine landslide

wave using their Boussinesq-type model, which has been used as a benchmark validation for predicting landslide waves [4,5]. A schematic view of the submarine-landslide-generated wave is shown in Fig. 4. Following the work of Lynett and Liu [2], the time-varying bottom topography is expressed as follows:

$$h(x,t) = sx - h'(x,t) \quad (11)$$

with

$$h'(x,t) = \frac{\Delta h}{4} [1 + \tanh(2(x - x_l(t)) \cos \theta)] [1 - \tanh(2(x - x_r(t)) \cos \theta)] \quad (12)$$

where Δh is the maximum vertical height of the slide; $s = \tan \theta$ is the bed slope; and $x_l(t)$ and $x_r(t)$ are given by

$$x_l(t) = x_c(t) - \frac{b}{2} \cos \theta, \quad x_r(t) = x_c(t) + \frac{b}{2} \cos \theta \quad (13)$$

with

$$x_c(t) = x_0 + S(t) \cos \theta \quad (14)$$

where x_0 is the initial position of landslide center of mass motion; $S(t)$ parallel to the slope is governed by the following expression:

$$S(t) = S_0 \ln \left[\cosh \left(\frac{t}{t_0} \right) \right] \quad (15)$$

with

$$S_0 = \frac{u_t^2}{a_0}, \quad t_0 = \frac{u_t}{a_0} \quad (16)$$

where a_0 and u_t are initial landslide acceleration and terminal landslide velocity, respectively and are determined by:

$$a_0 = g \frac{\gamma - 1}{\gamma + C_m} \sin \theta, \quad u_t = \sqrt{gb \frac{\pi(\gamma - 1)}{2C_d} \sin \theta} \quad (17)$$

where γ is the landslide specific density; C_m is an added mass coefficient; and C_d is a drag coefficient.

In our simulation, parameters presented by Fuhrman and Madsen [5] are adopted: $\Delta h = 0.05$ m, $\theta = 6^\circ$, $b = 1$ m, $x_0 = 2.379$ m, $\gamma = 2$, and $C_m = C_d = 1$. The

computational domain ranges from -1 m to 20 m in the x direction and the water depth ranges from 0 m at $x = 0$ m to 0.21 m at $x = 20$ m. Three horizontal grid sizes with $\Delta x = 0.1$ m, 0.05 m and 0.025 m are considered. Accordingly, the landslide is discretized by about 10, 20 and 40 divisions in the x direction. In the vertical direction, N_z is set to two, five and ten, respectively, to test the sensitivity of results to the number of horizontal layers.

Fig. 5 shows comparisons of the free-surface profiles between the three sets of numerical results with different horizontal grid sizes and the numerical results obtained by a boundary integral equation model (BIEM). The BIEM solves the potential flow equation in the vertical plane and predicts fully nonlinear and dispersive waves with high accuracy. The BIEM results can be found in the papers of Fuhrman and Madsen [5] and Lynett and Liu [2]. It can be seen from Fig. 5 that the present model results with $\Delta x = 0.05$ m and 0.025 m are quite similar and are in a good agreement with the BIEM results, demonstrating that grid convergence has been achieved by setting $\Delta x = 0.05$ m. Fig. 6 shows comparisons of the free-surface profiles between the three sets of numerical results with different numbers of horizontal layers and BIEM results. The present model results with five layers are quite similar to those with ten layers, indicating that grid convergence has been obtained after $N_z \geq 5$. Fig. 7 compares the hydrostatic model results and the non-hydrostatic model results to show the non-hydrostatic effects. The hydrostatic model is run by turning off the Poisson equation solver. In both hydrostatic and non-hydrostatic models, $\Delta x = 0.05$ m and $N_z = 5$ are employed. It can be seen from Fig. 7 that discrepancies between the hydrostatic and non-hydrostatic models become visible after $t = 3$ s. The non-hydrostatic model predicts larger values of the wave trough than the hydrostatic model at $t = 4.51$ s and 5.86 s. The non-hydrostatic effects play an important role in the generation of small oscillations behind the wave trough (see Fig. 7 (d)). Overall, the non-hydrostatic model results are in good agreement with the BIEM results.

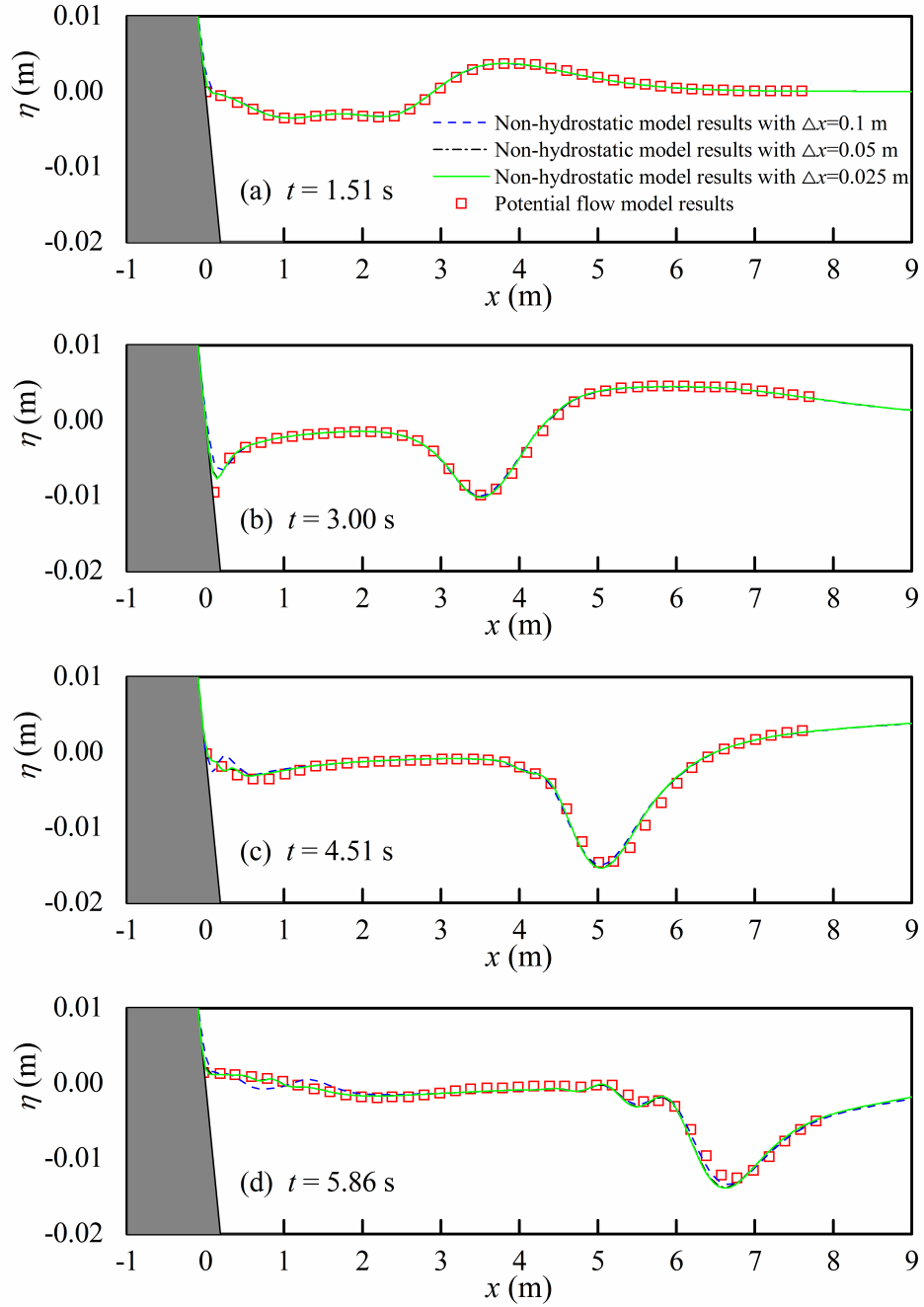


Fig. 5. Comparisons of free-surface profiles between the three sets of the non-hydrostatic model results with different horizontal grid sizes ($N_z = 5$) and BIEM results.

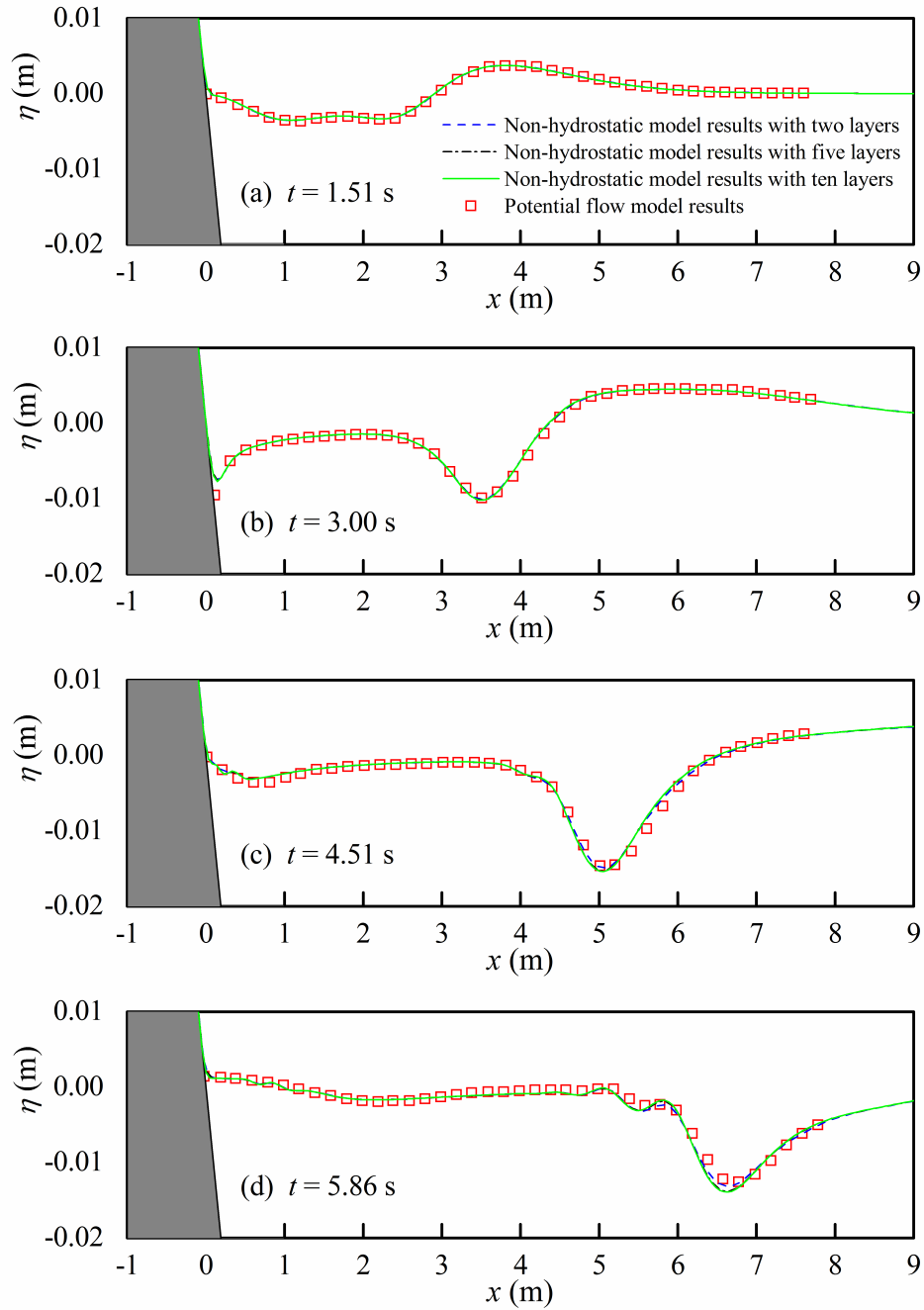


Fig. 6. Comparisons of free-surface profiles between the three sets of the non-hydrostatic model results with different numbers of horizontal layers ($\Delta x = 0.05$ m) and BIEM results.

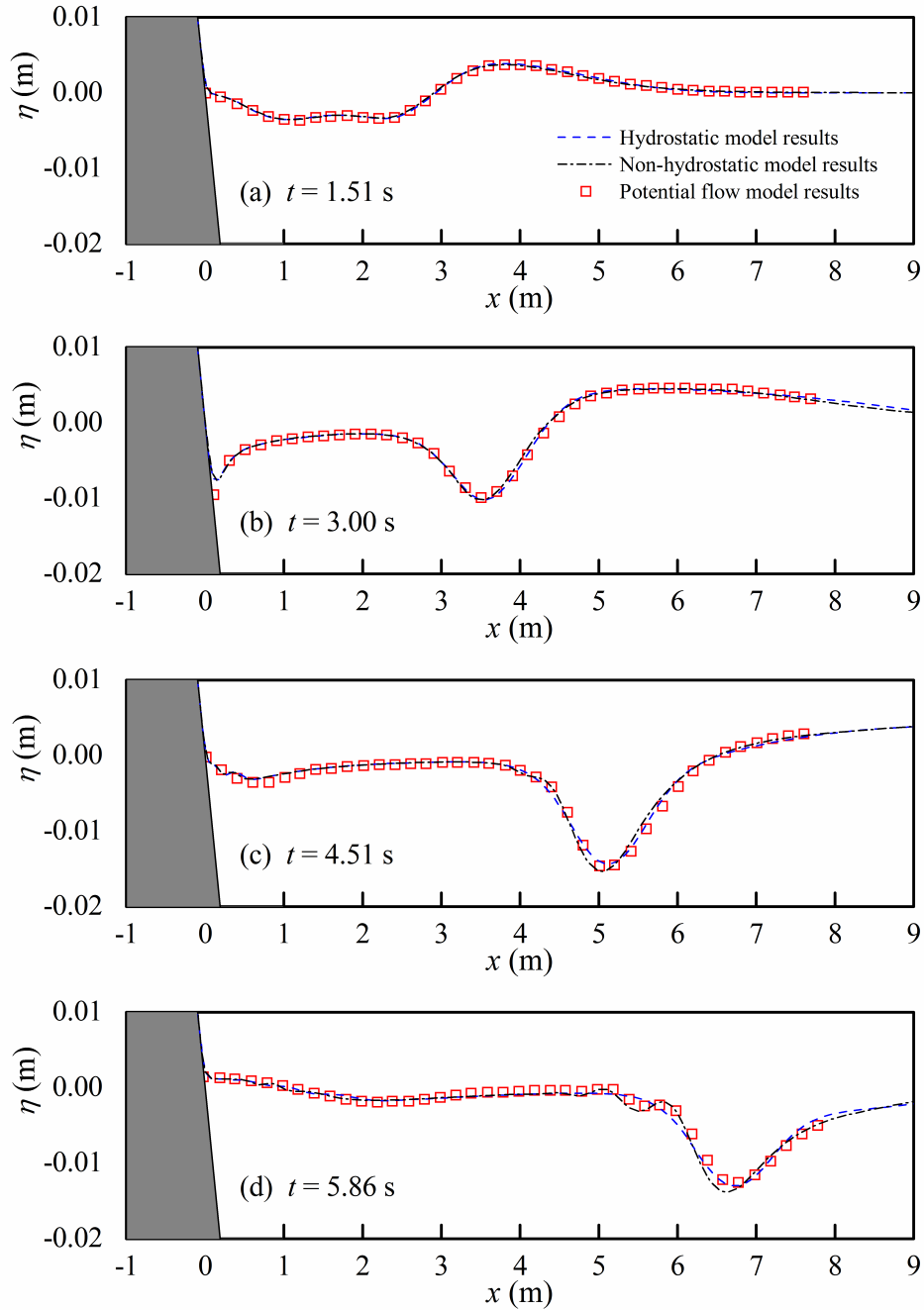


Fig. 7 Comparisons of free-surface profiles between hydrostatic model results, non-hydrostatic model results and BIEM results.

4.3 Experimental tsunami waves of Grilli et al. [7]

The experiment performed by Grilli et al. [7] was also a 2D vertical problem and has been selected as one of the benchmark tests by the NTHMP landslide tsunami benchmark workshop [36]. This test case has been used as a validation test for Boussinesq-type models [4,5] and potential flow models [7,8]. In their experiment, a

half-ellipse landslide was placed on a planar slope and after a while it slid into a flat region. A schematic view of Grilli et al.'s experiment [7] is shown in Fig. 8. The length and maximum thickness of the half-ellipse are $b = 1000$ m and $T = 52$ m, respectively. The planar slope is $\theta = 15^\circ$ and the water depth in the flat region is $h_0 = 1018.3$ m. The landslide center of mass motion parallel to the slope is also described by Eqs. (15) and (16). The initial landslide acceleration and terminal landslide velocity are $a_0 = 0.574 \text{ m/s}^2$ and $u_t = 45.91 \text{ m/s}$, respectively. The initial submergence depth of the landslide is $d = 161$ m, which leads to $x_0 = 1161.5$ m.

In the x direction, the computational domain is discretized by $\Delta x = 20$ m and the half-ellipse landslide is discretized by approximately 48 cells. Five horizontal layers are used in the vertical direction. The time step used in the simulation is set to $\Delta t = 0.1$ s. In Fig. 9, the time histories of present computed free-surface elevations are compared with the experimental data from Grilli et al. [7]. The high-order Boussinesq-type model results [5] and the numerical results from a potential flow model [7] are also superimposed in Fig. 9 for comparison. It should be emphasized that the time-varying bottom topography and the landslide motion employed in our simulation are identical to those used in Fuhrman and Madsen [5]. However, as described in Fuhrman and Madsen [5], to predict better results Grilli et al. [7] used landslide shape and motion that are slightly different from those used here. It can be seen from Fig. 9 that all of the numerical models predict reasonable results, when compared with the experimental data. However, the present model overpredicts the deep depression at $x = 1175$ m, while at other locations it accurately estimates the deep depression compared with other model results.

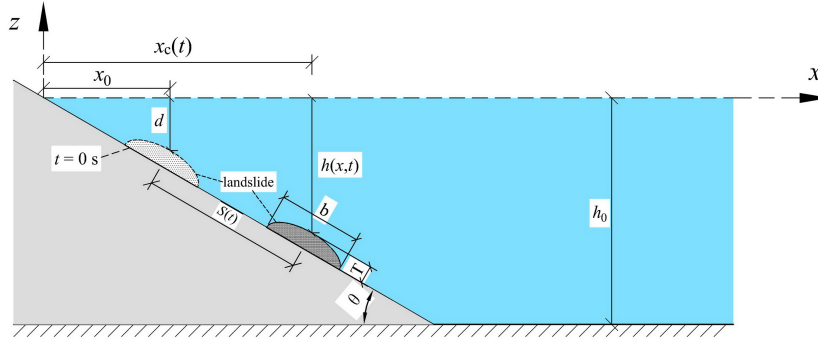


Fig. 8. Schematic diagram for the experimental set-up of Grilli et al. [7].

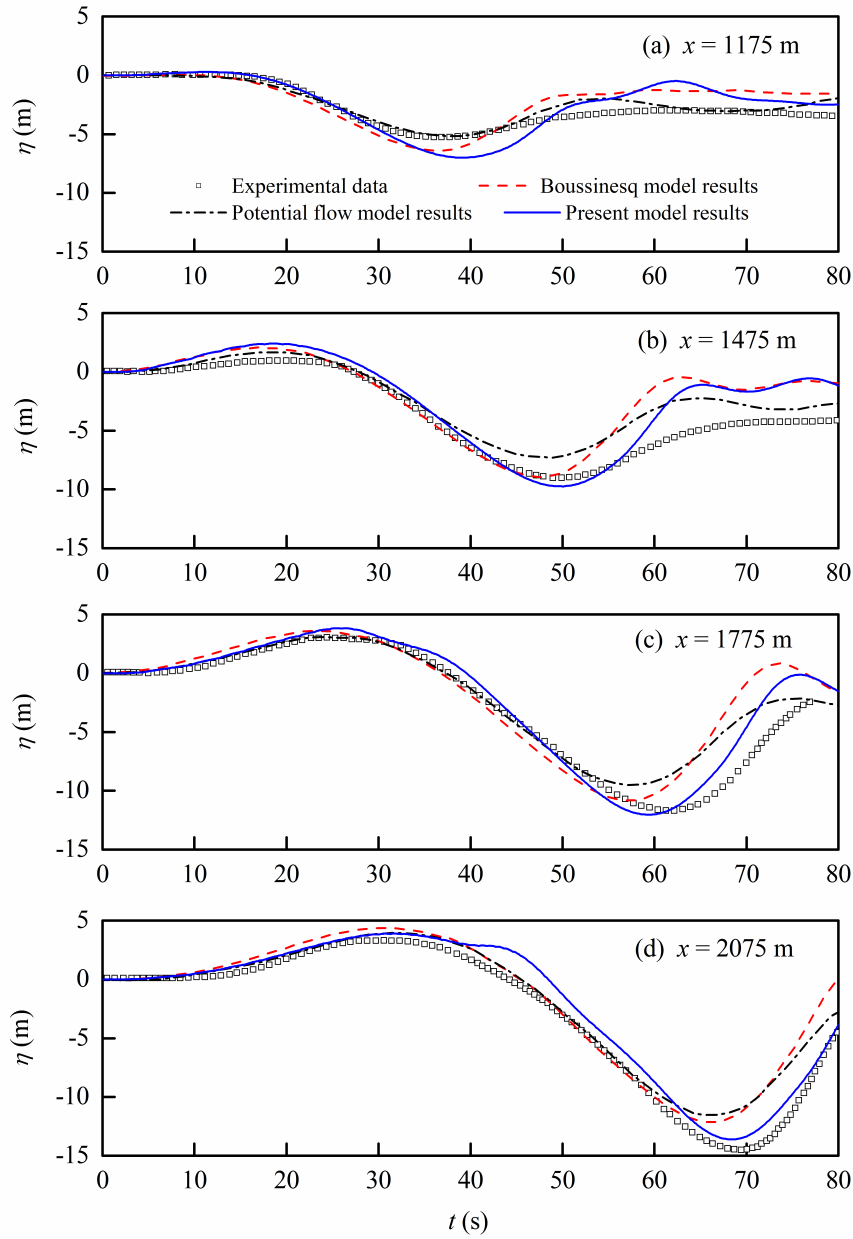


Fig. 9. Comparisons of time histories of the free-surface elevation at different locations among experimental data, present model results and numerical results obtained by the high-order Boussinesq-type model [5] and the potential flow model [7].

4.4 Experimental tsunami wave of Sue [9]

Sue [9] carried out a series of experiments for submarine-landslide-generated waves, which have been used as validations for the potential flow model developed at the University of Canterbury. In the experiments, a range of combinations of specific gravity and initial submergence of landslide were considered. In the present study, a test case named SG2_IS5 in Sue [9] is studied, which corresponds to a combination of moderate specific gravity with the shallowest initial submergence. A schematic view of Sue's experiments [9] can be found in Fig. 8. A half-ellipse landslide is also placed on a planar slope with $\theta = 15^\circ$, but there is a transition from the planar slope to a flat region, which allows the landslide to slide smoothly down the slope and then enter into the flat region. The length and the maximum thickness of the half-ellipse are $b = 0.5$ m and $T = 0.026$ m, respectively. Neglecting the landslide, the bottom topography can be described by following expressions:

For the planar slope ($0 \text{ m} \leq x < 1.297 \text{ m}$):

$$h(x) = x \tan \theta \quad (18)$$

For the transition ($1.297 \text{ m} \leq x < 1.807 \text{ m}$):

$$h(x) = -0.19(x - 1.297)^3 - 0.1024(x - 1.297)^2 + 0.2728(x - 1.297) + 0.3475 \quad (19)$$

For the flat region ($x \geq 1.807 \text{ m}$):

$$h(x) = h_0 \quad (20)$$

where the constant water depth $h_0 = 0.435$ m.

The initial position of the landslide center of mass motion is at $x_0 = 0.26$ m. Following Sue [9], the displacement $S(t)$ of the landslide parallel to the slope does not follow Eqs. (15) and (16) and is described by an idealized form, which divided the landslide motion into following three stages. In the first stage, the landslide slides down the slope with a constant acceleration a_0 until a time t_{\max} at which the landslide reaches the base of the slope. After this, the second stage starts, in which the

landslide moves along the flat region with a constant deceleration until a time t_{zero} , at which the landslide came into a rest. In the final stage, the landslide continues in a state of rest. Therefore, $S(t)$ is described as follows:

$$S(t) = \begin{cases} \frac{1}{2}a_0t^2 & \text{for } 0 \leq t \leq t_{max} \\ \frac{1}{2}a_0t_{max}^2 + a_0t_{max}(t - t_{max}) - a_0\frac{t_{max}}{2}\frac{(t - t_{max})^2}{(t_{zero} - t_{max})} & \text{for } t_{max} \leq t \leq t_{zero} \\ \frac{1}{2}a_0t_{max}^2 + \frac{1}{2}a_0t_{max}(t_{zero} - t_{max}) & \text{for } t \geq t_{zero} \end{cases} \quad (21)$$

where a_0 , t_{max} and t_{zero} are calculated from the landslide velocity time history, which was measured using Particle Tracking Velocimetry in the experiments. For the case of SG2_IS5, $a_0 = 1.004 \text{ m/s}^2$, $t_{max} = 1.265 \text{ s}$ and $t_{zero} = 6.045 \text{ s}$.

In the computation, the horizontal domain is discretized by $\Delta x = 0.025 \text{ m}$ and a time step $\Delta t = 0.02 \text{ s}$ is used. As a result, the landslide is discretized by approximately 19 horizontal cells. In the vertical direction, three horizontal layers are used. Fig. 10 compares the computed and measured free-surface profiles at various times. Fig. 11 compares time histories of the computed free-surface elevation with experimental data at various locations. It is found that the generation and propagation of the landslide-generated waves are well captured by the present model and generally good agreement is obtained between the model results and the measured data, further demonstrating the capability of the non-hydrostatic model in resolving landslide tsunami waves. The predicted main wave length for the generated waves is about 1.36 m (discretized by approximately 54 horizontal divisions), resulting in $Kh_0 \approx 2$.

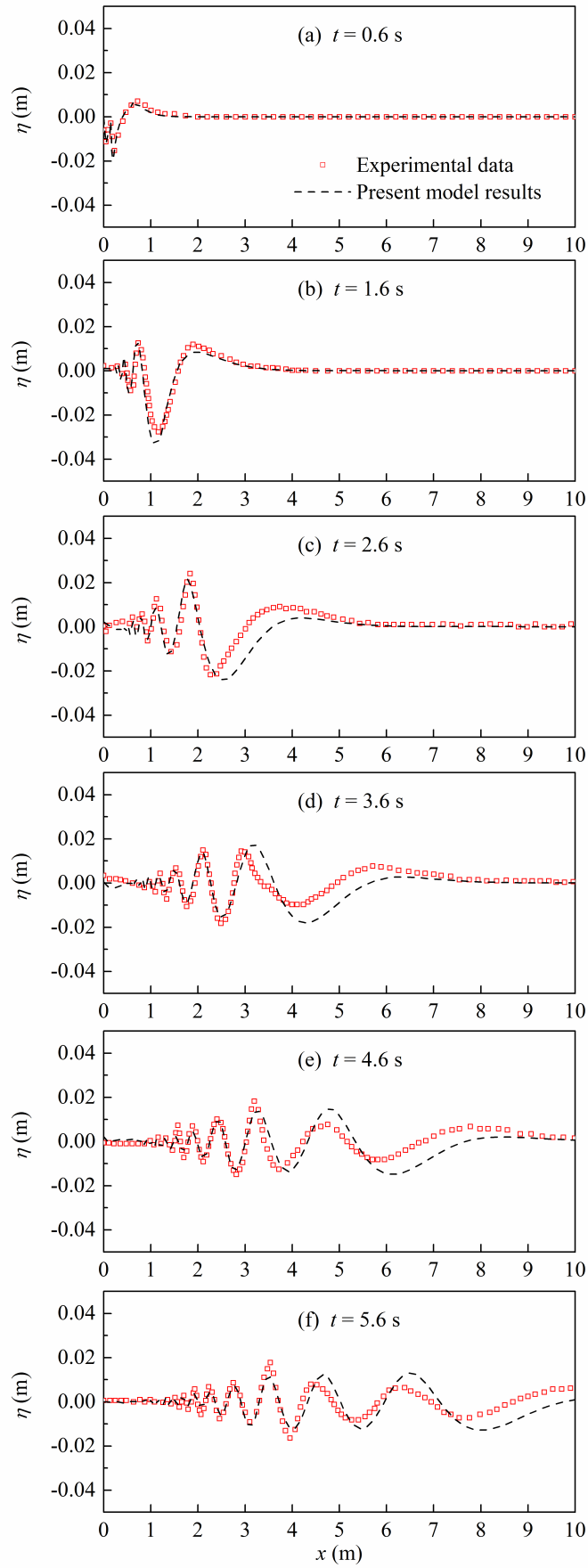


Fig. 10. Comparisons of free-surface profiles at various times between present model results and

experimental data from Sue [9].

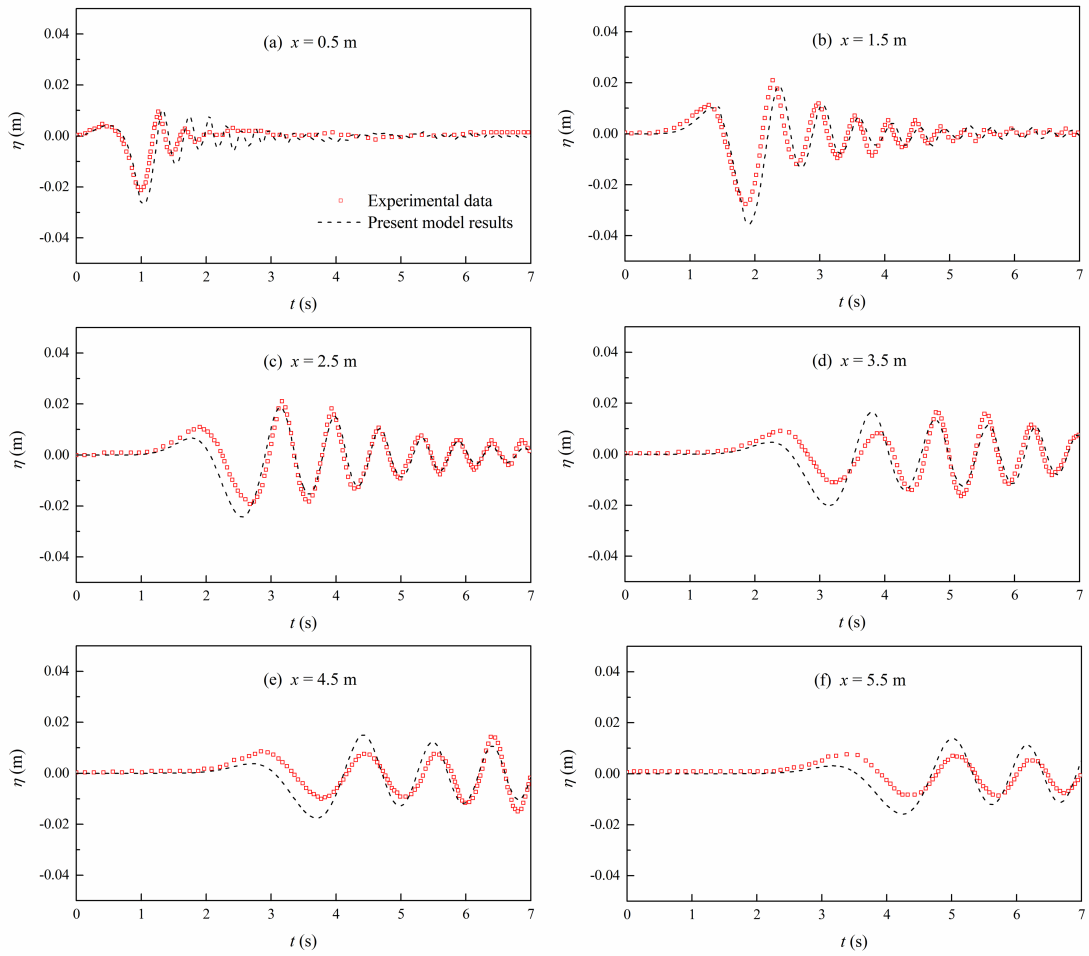


Fig. 11. Comparisons of time histories of the free-surface elevation at various locations between present model results and experimental data from Sue [9].

4.5 3D tsunami waves of Enet and Grilli [37]

As a final test, we conduct a numerical test for simulating tsunami waves generated by a 3D submarine landslide. The experimental data by Enet and Grilli [37] is adopted to validate the numerical results. This example is also one of the benchmark tests presented by the NTHMP landslide tsunami benchmark workshop [36]. The experiments performed by Enet and Grilli [37] generated highly dispersive waves and have been used for validating capabilities of dispersive numerical models [5,7,22] on resolving 3D tsunami waves. The experiments were carried out in the 3.7 m wide, 1.8 m deep, and 30 m long wave tank. A schematic diagram about the experimental setup is illustrated in Fig. 12. In this figure, only a local coordinate

system (x', y', z') is plotted. The global coordinate system (x, y, z) defined in this test is analogous to that shown in Fig. 8, in which the origin of the coordinate is located in the shoreline and $y = 0$ m is the symmetric plane of the computational domain.

A Gaussian shaped landslide with length $b = 0.395$ m, width $w = 0.68$ m, and thickness $T = 0.082$ m is placed on a planar slope with $\theta = 15^\circ$. The landslide geometry is defined using the following truncated hyperbolic secant functions in the coordinates oriented with the planar slope:

$$z' = \frac{T}{1 - \varepsilon} [\text{sech}(k_b x') \text{sech}(k_w y') - \varepsilon] \quad (22)$$

where $k_b = 2C/b$; $k_w = 2C/w$; $C = \text{acosh}(1/\varepsilon)$; and $\varepsilon = 0.717$ is the truncation parameter.

The water depth in the flat region is maintained constant as $h_0 = 1.5$ m. For the displacement $S(t)$ of the landslide parallel to the slope, it is also described by Eqs. (15) and (16). Three test cases with different initial submergences of landslide are considered in this study. Parameters used in each case are listed in Table 1.

Table 1. Summary of parameters used in each case for the 3D experimental tsunami waves of Enet and Grilli [37]

Case	d (mm)	a_0 (m/s ²)	u_t (m/s)
A	61	1.12	1.70
B	120	1.17	2.03
C	189	1.21	1.97

In the numerical computations, following Fuhrman and Madsen [5], the horizontal domain is discretized by setting the grid interval length $\Delta x = 0.025$ m and $\Delta y = 0.04625$ m and the time step is $\Delta t = 0.005$ s. The landslide is discretized by approximately 15 and 14 divisions in the x and y directions, respectively. Five horizontal layers are used in the vertical direction. The computational domain is 10 m

long and 3.7 m wide. For the three test cases, comparisons of free-surface elevations at various locations between present model results, numerical results obtained by the high-order Boussinesq-type model [5] and experimental data from Enet and Grilli [37] are shown in Figs. 13-15. As described in Enet and Grilli [37], experimental data are not available at the gauging point (1.929, 0) m for Case B because of a data-logger problem. The estimated main wave lengths for Case A, Case B and Case C are 0.96 m, 1.01 m and 1.05 m, respectively and are discretized by approximately 38, 40 and 42 horizontal divisions, respectively. It can be found that with the increase in the initial submergence, discrepancies between present model results and measured data become more visible. However, numerical predictions are in generally good agreement with experiments. The present model behaves better than the high-order Boussinesq-type model for Case A, in which the high-order Boussinesq-type model overestimates the wave crest. For Case B and Case C, both model results are similar.

Fig. 16 shows the time evolution of the wave field for Case A, which results in the largest waves of the three test cases considered. The generated waves are characterized by a relatively larger leading wave, followed by a dispersive wave train and have very notable 3D effects. At the time $t = 1$ s, a short-crested leading wave was formed. Hereafter, the leading wave crest becomes wider and lower.

To illustrate the 3D feature of the test cases, Fig. 17 shows distributions of the normalized non-hydrostatic pressures and velocities in the symmetric plane of $y = 0$ at a typical time $t = 2.5$ s for Case A. It can be seen that distributions of the non-hydrostatic pressures and the horizontal velocities in the vicinity of the landslide are almost identical. There are negative values above the landslide, while positive ones can be detected in front of or in the rear of the landslide. For the distribution of vertical velocities, there are positive and negative values in tandem appearing above the landslide.

The computational efficiency for the three test cases is shown in Table 2. The model was run on a notebook computer with Intel Core (TM) i7-5700HQ CPU. The CPU is a quad-core processor and has a base frequency of 2.7 GHz with 6MB L3

cache. The model uses the C# shared memory library for parallelization. The total CPU times for Case A, Case B and Case C are 266.50 s, 314.46 s and 295.61 s, respectively.

Table 2 Computational efficiency for the 3D experimental tsunami waves of Enet and Grilli [37]

Case	Computational environment	Simulation time (s)	Total grid number	CPU time (s)
A	CPU: Intel Core (TM) i7-5700HQ, 4 cores, 2.7 GHz;	3.5	160,000	266.50
B	L3: 6 MB			314.46
C				295.61

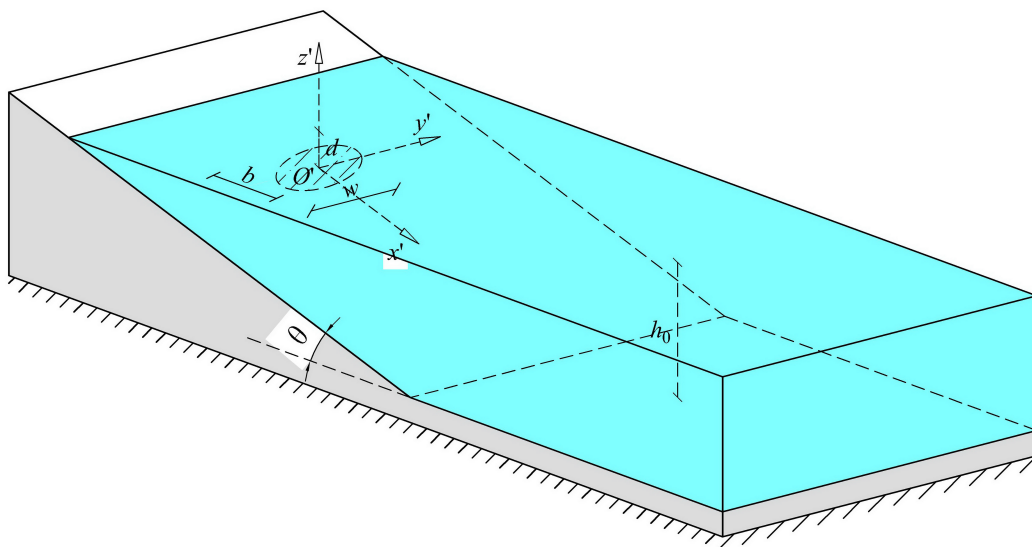


Fig. 12. Schematic diagram for the experimental set-up of Enet and Grilli [37].

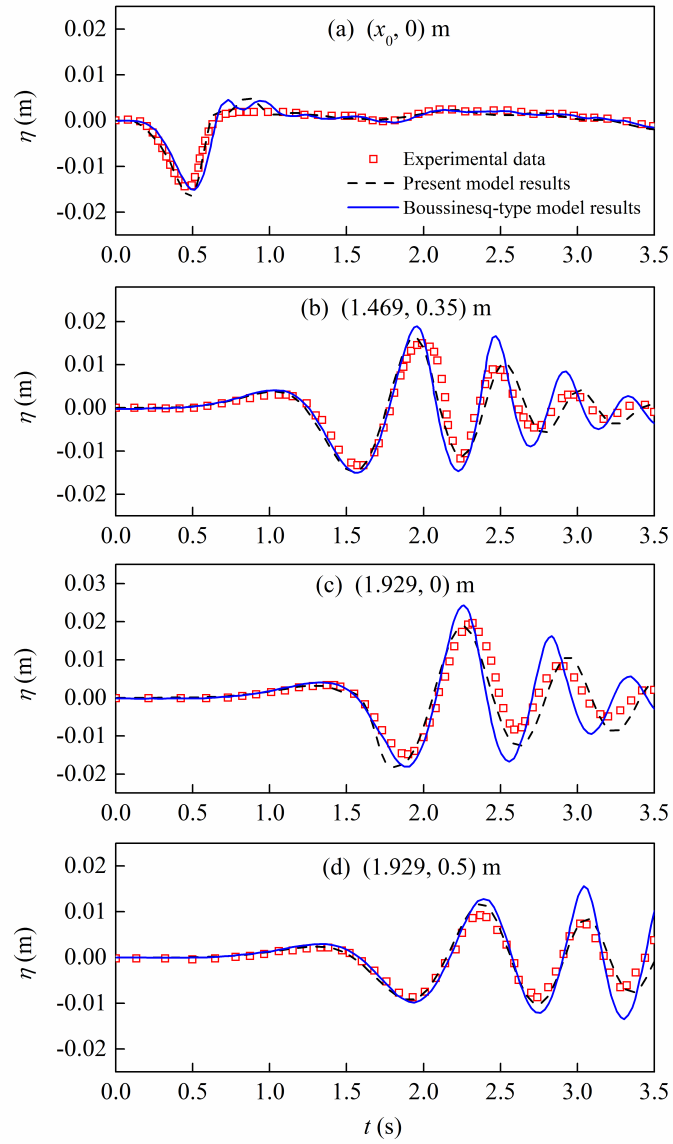


Fig. 13. Comparisons of the free-surface elevation at various locations between the present model results, the numerical results obtained by the high-order Boussinesq-type model [5] and experimental data for Case A.

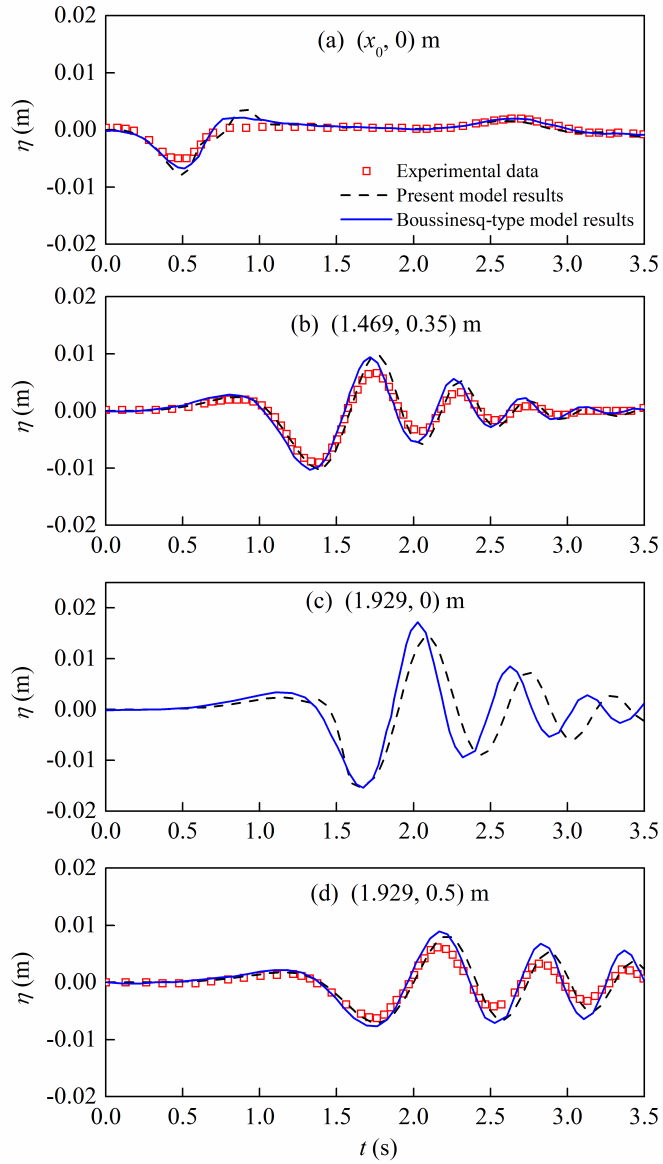


Fig. 14. Comparisons of the free-surface elevation at various locations between the present model results, the numerical results obtained by the high-order Boussinesq-type model [5] and experimental data for Case B.

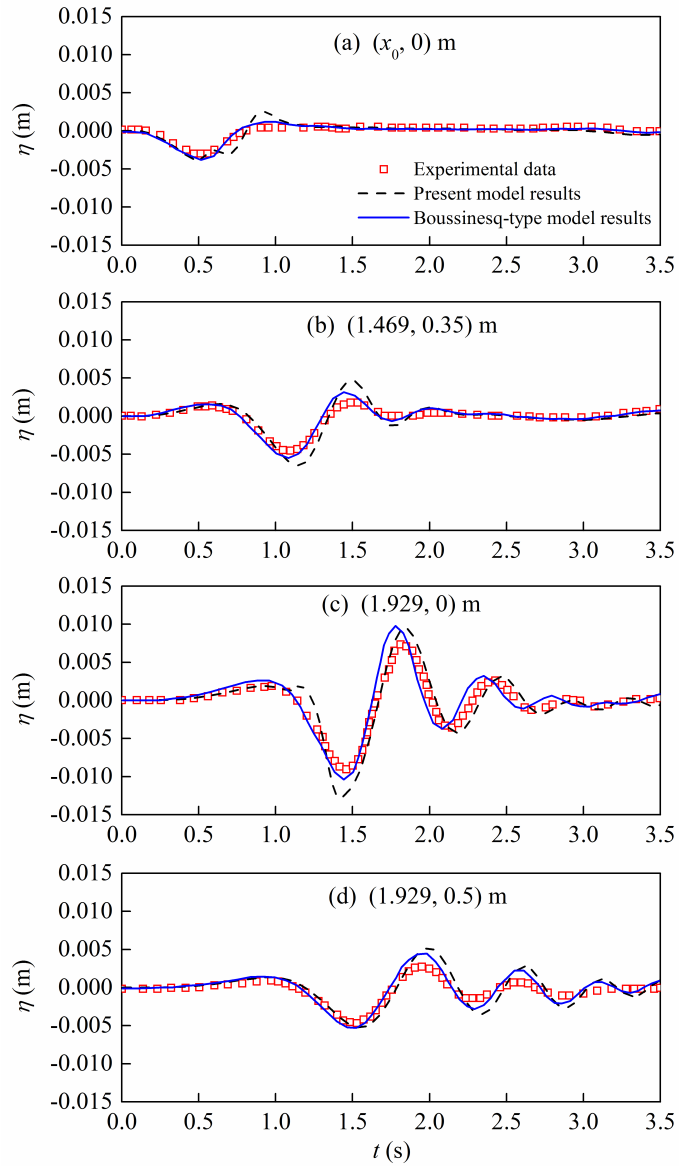


Fig. 15. Comparisons of the free-surface elevation at various locations between the present model results, the numerical results obtained by the high-order Boussinesq-type model [5] and the experimental data for Case C.

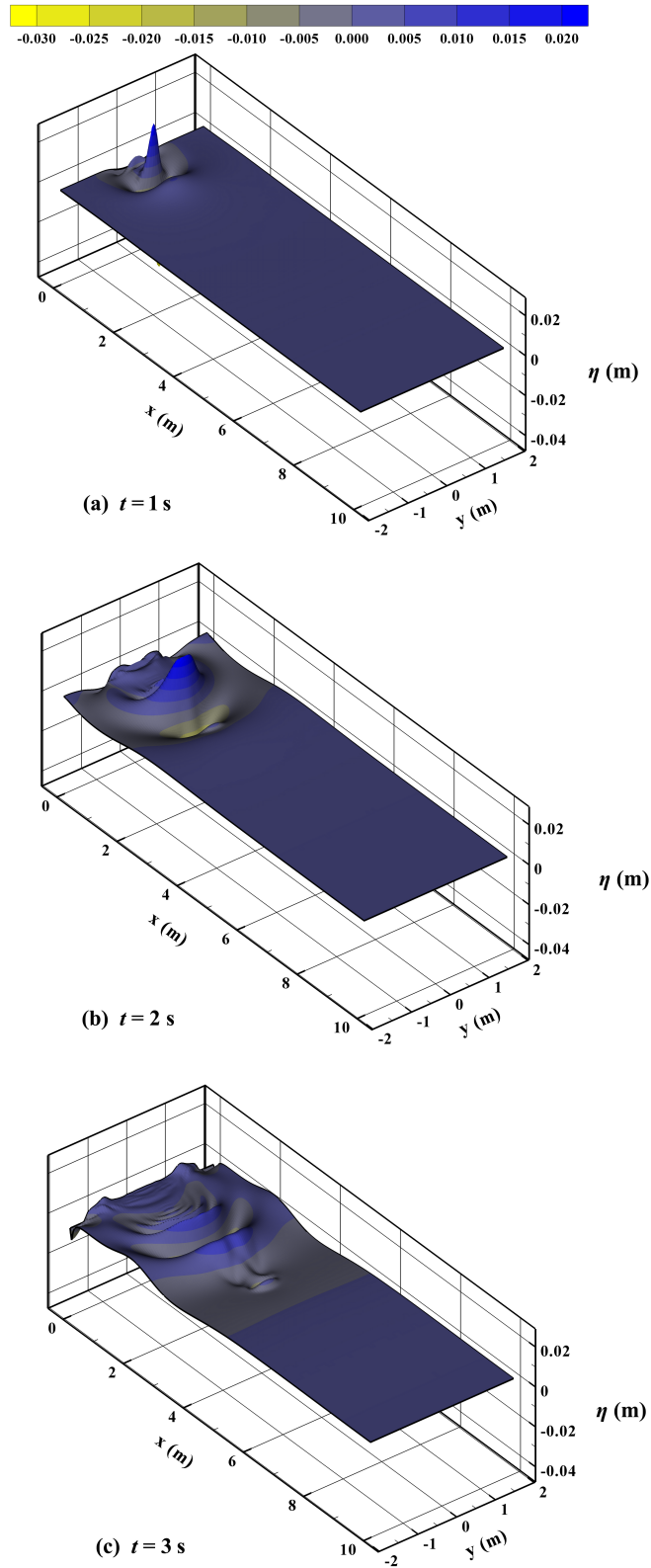


Fig. 16. 3D view plots of the free-surface elevation at representative times for Case A.

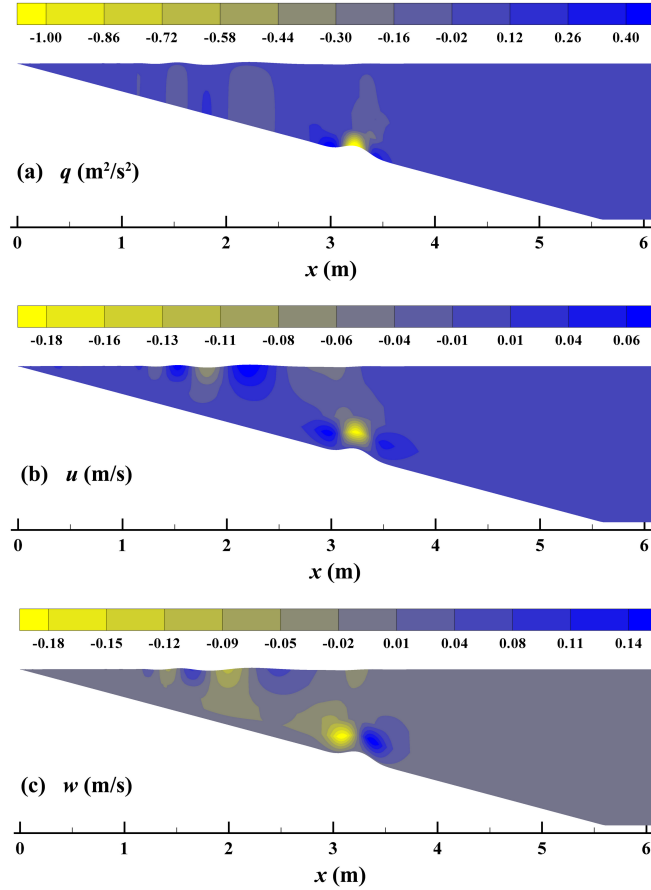


Fig. 17. Distributions of the normalized non-hydrostatic pressure q , horizontal velocity u , and vertical velocity w in the symmetric plane of $y=0$ at the time $t=2.5$ s for Case A. (The vertical scale is the same as the horizontal one.)

5. Conclusions

This paper presents a 3D non-hydrostatic model for simulating nonlinear and dispersive waves to predict submarine-landslide-generated waves. The model is developed by incorporating the moving bottom boundary into the projection method, which is utilized to solve the 3D Navier-Stokes equations. The resulting Poisson equation for non-hydrostatic pressure correction terms is also symmetric. Thus, the 3D model is also computationally efficient, because the preconditioned conjugate gradient method can be employed to solve the Poisson equation.

A wide range of numerical tests involving tsunami waves generated by 2D or 3D landslides are used to validate the developed model. In the first two tests of 2D

tsunami waves, it is found that very good agreements are obtained between present model results and those obtained by the high-order Boussinesq-type model [5] or the potential flow model [2]. In the test of experimental tsunami wave of Grilli et al. [7], the present non-hydrostatic model behaves better than the high-order Boussinesq-type model [5] and the potential flow model [7] in the prediction of deep depression of waves. For the test of experimental tsunami waves of Sue [9], the non-hydrostatic model captures the generation and propagation of the landslide-generated waves well and agreements between model results and experimental data are generally good. In the final 3D example, numerical predictions are also in generally good agreement with experiments and the 3D feature of the generated tsunami wave is revealed. Overall, all the validations demonstrate the developed model's capability for resolving landslide waves and the model can be considered as an attractive alternative to predicting 3D tsunami waves induced by submarine landslides.

In the present model, landslides are considered as rigid blocks which limits the model's applicability. The model [18] can be extended to predict tsunami waves induced by deformable submarine landslides following the work of Ma et al. [28], in which landslides are treated as water-sediment mixtures. The model [18] also can be coupled with a depth-averaged granular flow model to simulate tsunami wave generation by granular slides following Ma et al. [30] or Macías et al. [31].

Acknowledgement

This research is financially supported by the National Natural Science Foundation of China (Grant No. 51679031, 51979029, 51720105010), LiaoNing Revitalization Talents Program (Grant No. XLYC1807010) and the Fundamental Research Funds for the Central Universities (Grant No. DUT2019TB02).

References

- [1] C.B. Harbitz, Model simulations of tsunamis generated by the Storegga slides, *Marine Geol.* 105 (1992) 1-21. [https://doi.org/10.1016/0025-3227\(92\)90178-K](https://doi.org/10.1016/0025-3227(92)90178-K).
- [2] P. Lynett, P.L.-F. Liu, A numerical study of submarine landslide generated waves and run-up, *Proc. R. Soc. London. Ser. A Math. Phys. Eng. Sci.* 458 (2002) 2885–2910. <https://doi.org/10.1098/rspa.2002.0973>.
- [3] S. Yavari-Ramshe, B. Ataie-Ashtiani, Numerical modeling of subaerial and submarine landslide-generated tsunami waves—recent advances and future challenges, *Landslides.* 13 (2016) 1325–1368. <https://doi.org/10.1007/s10346-016-0734-2>.
- [4] B. Ataie-Ashtiani, A. Najafi Jilani, A higher-order Boussinesq-type model with moving bottom boundary: applications to submarine landslide tsunami waves, *Int. J. Numer. Methods Fluids.* 53 (2007) 1019–1048. <https://doi.org/10.1002/flid.1354>.
- [5] D.R. Fuhrman, P.A. Madsen, Tsunami generation, propagation, and run-up with a high-order Boussinesq model, *Coast. Eng.* 56 (2009) 747–758. <https://doi.org/10.1016/j.coastaleng.2009.02.004>.
- [6] S.T. Grilli, P. Watts, Modeling of waves generated by a moving submerged body. Applications to underwater landslides, *Eng. Anal. Bound. Elem.* 23 (1999) 645–656. [https://doi.org/10.1016/S0955-7997\(99\)00021-1](https://doi.org/10.1016/S0955-7997(99)00021-1).
- [7] S.T. Grilli, S. Vogelmann, P. Watts, Development of a 3D numerical wave tank for modeling tsunami generation by underwater landslides, *Eng. Anal. Bound. Elem.* 26 (2002) 301–313. [https://doi.org/10.1016/S0955-7997\(01\)00113-8](https://doi.org/10.1016/S0955-7997(01)00113-8).
- [8] S.T. Grilli, P. Watts, Tsunami generation by submarine mass failure. I: Modeling, experimental validation and sensitivity analyses, *J. Waterw. Port, Coast. Ocean Eng.* 131 (2005) 283–297. [https://doi.org/10.1061/\(ASCE\)0733-950X\(2005\)131:6\(283\)](https://doi.org/10.1061/(ASCE)0733-950X(2005)131:6(283))
- [9] L.P. Sue, Modelling of tsunami generated by submarine landslides, University of Canterbury, 2007 Ph.D. thesis.

- [10] S. Abadie, D. Morichon, S. Grilli, S. Glockner, Numerical simulation of waves generated by landslides using a multiple-fluid Navier-Stokes model, *Coast. Eng.* 57 (2010) 779–794. <https://doi.org/10.1016/j.coastaleng.2010.03.003>.
- [11] B. Ataie-Ashtiani, G. Shobeyri, Numerical simulation of landslide impulsive waves by incompressible smoothed particle hydrodynamics, *Int. J. Numer. Methods Fluids.* 56 (2008) 209–232. <https://doi.org/10.1002/flid.1526>.
- [12] G. Li, G. Chen, P. Li, H. Jing, Efficient and accurate 3-D numerical modelling of landslide Tsunami, *Water (Switzerland)*. 11 (2019) 1–17. <https://doi.org/10.3390/w11102033>.
- [13] P.L.F. Liu, T.R. Wu, F. Raichlen, C.E. Synolakis, J.C. Borrero, Runup and rundown generated by three-dimensional sliding masses, *J. Fluid Mech.* 536 (2005) 107–144. <https://doi.org/10.1017/S0022112005004799>.
- [14] D. Yuk, S.C. Yim, P.L.F. Liu, Numerical modeling of submarine mass-movement generated waves using RANS model, *Comput. Geosci.* 32 (2006) 927–935. <https://doi.org/10.1016/j.cageo.2005.10.028>.
- [15] T. Capone, A. Panizzo, J.J. Monaghan, SPH modelling of water waves generated by submarine landslides, *J. Hydraul. Res.* 48 (2010) 80–84. <https://doi.org/10.1080/00221686.2010.9641248>.
- [16] B.E. Snelling, G.S. Collins, M.D. Piggott, S.J. Neethling, Improvements to a smooth particle hydrodynamics simulator for investigating submarine landslide generated waves, *Int. J. Numer. Methods Fluids.* 92 (2020) 744–764. <https://doi.org/10.1002/flid.4804>.
- [17] C. Ai, S. Jin, A multi-layer non-hydrostatic model for wave breaking and run-up, *Coast. Eng.* 62 (2012) 1–8. <https://doi.org/10.1016/j.coastaleng.2011.12.012>.
- [18] C. Ai, S. Jin, B. Lv, A new fully non-hydrostatic 3D free surface flow model for water wave motions, *Int. J. Numer. Methods Fluids.* 66 (2011) 1354–1370. <https://doi.org/10.1002/flid.2317>.
- [19] C. Ai, W. Ding, S. Jin, A general boundary-fitted 3D non-hydrostatic model for nonlinear focusing wave groups, *Ocean Eng.* (2014) 134–145.

- <https://doi.org/10.1016/j.oceaneng.2014.08.002>.
- [20] C. Ai, Y. Ma, C. Yuan, G. Dong, Development and assessment of semi-implicit nonhydrostatic models for surface water waves, *Ocean Model.* 144 (2019) 101489. <https://doi.org/10.1016/j.ocemod.2019.101489>.
- [21] H. Cui, J.D. Pietrzak, G.S. Stelling, Improved efficiency of a non-hydrostatic, unstructured grid, finite volume model, *Ocean Model.* 54–55 (2012) 55–67. <https://doi.org/10.1016/j.ocemod.2012.07.001>.
- [22] G. Ma, F. Shi, J.T. Kirby, Shock-capturing non-hydrostatic model for fully dispersive surface wave processes, *Ocean Model.* 43–44 (2012) 22–35. <https://doi.org/10.1016/j.ocemod.2011.12.002>.
- [23] C.C. Young, C.H. Wu, Nonhydrostatic modeling of nonlinear deep-water wave groups, *J. Eng. Mech.* 136 (2010) 155–167. [https://doi.org/10.1061/\(ASCE\)EM.1943-7889.0000078](https://doi.org/10.1061/(ASCE)EM.1943-7889.0000078).
- [24] M. Zijlema, G. Stelling, P. Smit, SWASH: An operational public domain code for simulating wave fields and rapidly varied flows in coastal waters, *Coast. Eng.* 58 (2011) 992–1012. <https://doi.org/10.1016/j.coastaleng.2011.05.015>.
- [25] G. Ruffini, V. Heller, R. Briganti, Numerical modelling of landslide-tsunami propagation in a wide range of idealised water body geometries, *Coast. Eng.* 153 (2019) 103518. <https://doi.org/10.1016/j.coastaleng.2019.103518>.
- [26] J. Hill, G.S. Collins, A. Avdis, S.C. Kramer, M.D. Piggott, How does multiscale modelling and inclusion of realistic palaeobathymetry affect numerical simulation of the Storegga Slide tsunami?, *Ocean Model.* 83 (2014) 11–25. <https://doi.org/10.1016/j.ocemod.2014.08.007>.
- [27] W. Pan, S.C. Kramer, T. Kärnäb, M.D. Piggott, Comparing non-hydrostatic extensions to a discontinuous finite element coastal ocean model, *Ocean Model.* 151 (2020) 101634. <https://doi.org/10.1016/j.ocemod.2020.101634>.
- [28] G. Ma, J.T. Kirby, F. Shi, Numerical simulation of tsunami waves generated by deformable submarine landslides, *Ocean Model.* 69 (2013) 146–165. <https://doi.org/10.1016/j.ocemod.2013.07.001>.
- [29] R.C. Smith, J. Hill, G.S. Collins, M.D. Piggott, S.C. Kramer, S.D. Parkinson, C.

- Wilson, Comparing approaches for numerical modelling of tsunami generation by deformable submarine slides, *Ocean Model.* 100 (2016) 125–140. <https://doi.org/10.1016/j.ocemod.2016.02.007>.
- [30] G. Ma, J.T. Kirby, T.-J. Hsu, F. Shi, A two-layer granular landslide model for tsunami wave generation: Theory and computation, *Ocean Model.* 93 (2015) 40–55. <https://doi.org/10.1016/j.ocemod.2015.07.012>.
- [31] J. Macías, C. Escalante, M.J. Castro, Multilayer-HySEA model validation for landslide generated tsunamis. Part II Granular slides, *Nat. Hazards Earth Syst. Sci. Discuss.* (2020) 1–34. <https://doi.org/10.5194/nhess-2020-172>.
- [32] S.T. Grilli, D.R. Tappin, S. Carey, S.F.L. Watt, S.N. Ward, A.R. Grilli, S.L. Engwell, C. Zhang, J.T. Kirby, L. Schambach, M. Muin, Modelling of the tsunami from the December 22, 2018 lateral collapse of Anak Krakatau volcano in the Sunda Straits, Indonesia, *Sci. Rep.* 9 (2019) 11946. <https://doi.org/10.1038/s41598-019-48327-6>.
- [33] J. Smagorinsky, General circulation experiments with primitive equation I. The basic experiment, *Mon. Weather Rev.* 91 (1963) 99–164.
- [34] C. Ai, S. Jin, Non-hydrostatic finite volume model for non-linear waves interacting with structures, *Comput. Fluids.* 39 (2010) 2090–2100. <https://doi.org/10.1016/j.compfluid.2010.08.006>.
- [35] J.L. Hammack, A note on tsunamis: their generation and propagation in an ocean of uniform depth, *J. Fluid Mech.* 60 (1973) 769–799. <https://doi.org/10.1017/S0022112073000479>.
- [36] J.T. Kirby, S.T. Grilli, C. Zhang, J. Horrillo, D. Nicolsky, P.L.-F. Liu, The NTHMP landslide tsunami benchmark workshop, Galveston, January 9-11, Tech. Rep., Center for Applied Coastal Research, USA, 2017.
- [37] F. Enet, T. Grilli, Experimental study of tsunami generation by three-dimensional rigid underwater landslides, *J. Waterw. Port, Coast. Ocean Eng.* 133 (2007) 442–454. [https://doi.org/10.1061/\(ASCE\)0733-950X\(2007\)133:6\(442\)](https://doi.org/10.1061/(ASCE)0733-950X(2007)133:6(442)).